

# Geochemistry, Geophysics, Geosystems®



## RESEARCH ARTICLE

10.1029/2021GC010130

## Duration and Intensity of End-Permian Marine Anoxia

Michael Pimentel-Galvan<sup>1</sup> , Kimberly V. Lau<sup>2</sup>, Katharine Maher<sup>3</sup> , Tapan Mukerji<sup>4</sup>,  
Daniel J. Lehrmann<sup>5</sup> , Demir Altiner<sup>6</sup>, and Jonathan L. Payne<sup>1</sup> 

### Key Points:

- Uranium cycle models are run using the Monte Carlo method and compared to existing data to quantify the best-fitting history of ocean anoxia and its associated uncertainty
- A temporary increase in anoxia to  $18\% \pm 4\%$  of the seafloor followed by a million-year-long episode of  $7\% \pm 4\%$  seafloor anoxia explain trends within uranium isotope and concentration data
- Seafloor anoxia persisted at levels far above modern for at least 1.7 Mya after the end-Permian extinction event

### Supporting Information:

Supporting Information may be found in the online version of this article.

### Correspondence to:

M. Pimentel-Galvan,  
[michaelpimentel65@gmail.com](mailto:michaelpimentel65@gmail.com)

### Citation:

Pimentel-Galvan, M., Lau, K. V., Maher, K., Mukerji, T., Lehrmann, D. J., Altiner, D., & Payne, J. L. (2022). Duration and intensity of end-Permian marine anoxia. *Geochemistry, Geophysics, Geosystems*, 23, e2021GC010130. <https://doi.org/10.1029/2021GC010130>

Received 30 AUG 2021

Accepted 23 NOV 2021

### Author Contributions:

**Conceptualization:** Kimberly V. Lau, Katharine Maher, Tapan Mukerji, Daniel J. Lehrmann, Demir Altiner, Jonathan L. Payne

**Data curation:** Michael Pimentel-Galvan

**Formal analysis:** Michael Pimentel-Galvan, Tapan Mukerji, Jonathan L. Payne

**Funding acquisition:** Jonathan L. Payne

**Investigation:** Michael Pimentel-Galvan, Kimberly V. Lau, Katharine Maher,

<sup>1</sup>Department of Geological Sciences, Stanford University, Stanford, CA, USA, <sup>2</sup>Department of Geosciences, Pennsylvania State University, University Park, PA, USA, <sup>3</sup>Department of Earth System Science, Stanford University, Stanford, CA, USA, <sup>4</sup>Department of Energy Resources Engineering, Stanford University, Stanford, CA, USA, <sup>5</sup>Department of Geosciences, Trinity University, San Antonio, TX, USA, <sup>6</sup>Department of Geological Engineering, Middle East Technical University, Ankara, Turkey

**Abstract** Ocean anoxia was an important kill mechanism in the end-Permian mass extinction and uranium isotope data are among the most powerful tools for quantifying the global extent and duration of ocean deoxygenation due to the dependence of uranium isotope fractionation on bottom-water redox conditions. Although coherent stratigraphic variation in uranium isotope ratios ( $\delta^{238}\text{U}$ ) and uranium concentrations ([U]) indicative of prolonged deoxygenation beginning coincident with the extinction is well established, the precise extent of anoxia and associated uncertainty have yet to be quantified. Uncertainty arises from both noise in the data and imprecise knowledge of key parameters within the uranium cycle. In this study, we use the Monte Carlo method to explore a range of scenarios and their implications for the uranium cycle across the Permian-Triassic boundary and through the first 1.7 million years of the Triassic. We then compare model predictions against measured data using principal component analysis to identify model runs and associated parameter values most compatible with trends in the observed data. The best-fitting models indicate a pronounced increase in the extent of seafloor anoxia across the Permian/Triassic transition, reaching 18% of the seafloor (95% CI: [11%, 47%]), lasting anywhere from 20 kyr to 1.2 Myr. There is an inverse relationship between the extent and duration of anoxia in the set of best-fitting models. This initial pulse of pronounced anoxia is followed by a prolonged aftermath, which continues through the remainder of the study interval, of less extensive, yet still expanded, anoxia covering 7.8% of the seafloor (95% CI: [1.6%, 48.9%]). Both expanded and protracted anoxia are required to fit existing data, with no indication of full re-oxygenation during the study interval.

**Plain Language Summary** Uranium content and isotope composition in marine limestone provide strong evidence for a rapid reduction of oxygen availability in seawater coincident with the end-Permian mass extinction and lasting for hundreds of thousands of years. Visual comparison to forward model output for the uranium cycle has previously demonstrated that expanded marine anoxia is the best explanation for trends in the data but statistical best estimates of the extent and duration of anoxia as well as the uncertainty in those values have yet to be developed. Here, Monte Carlo simulations are used to predict uranium concentrations and isotope compositions for marine limestones under a wide range of scenarios. These simulations are then compared to published uranium data to identify the model runs that best fit the observed data. The results favor simulations with either short (~25 kyr), intense intervals of anoxia (~20% of the seafloor), or longer intervals (~1 Myr) with less extensive anoxia (~10%). Both situations are followed by a prolonged period of still-expanded but less extensive anoxia that vary depending on the intensity and duration of the initial perturbation (~1%–48%).

## 1. Introduction

The end-Permian mass extinction event eliminated approximately 80% of marine animal genera (Payne & Clapham, 2012) and permanently altered the taxonomic composition and ecological structure of Earth's biota (Bambach et al., 2002; Sepkoski, 1981). Physiological stresses imposed by ocean deoxygenation, ocean acidification, and global warming have long been hypothesized as important causes of biodiversity loss (Hallam, 1991; Wignall & Hallam, 1992; Wignall & Twitchett, 1996) and more recent analyses suggest that these stresses can explain the taxonomic (Knoll et al., 1996, 2007) and biogeographic (Penn et al., 2018) selectivity of the event.

The combination of Earth system model simulations with quantitative constraints on the ecophysiological traits of marine animals has opened an opportunity to compare observed extinction patterns with quantitative predictions (Penn et al., 2018) and such approaches will likely soon enable similar investigation of the ways in

© 2021 The Authors.

This is an open access article under the terms of the [Creative Commons Attribution-NonCommercial License](https://creativecommons.org/licenses/by-nc/4.0/), which permits use, distribution and reproduction in any medium, provided the original work is properly cited and is not used for commercial purposes.

Daniel J. Lehrmann, Demir Altiner,  
Jonathan L. Payne  
**Methodology:** Michael Pimentel-Galvan,  
Tapan Mukerji, Jonathan L. Payne  
**Project Administration:** Jonathan L.  
Payne  
**Software:** Michael Pimentel-Galvan,  
Tapan Mukerji, Jonathan L. Payne  
**Supervision:** Kimberly V. Lau, Jonathan  
L. Payne  
**Validation:** Kimberly V. Lau, Katharine  
Maher, Jonathan L. Payne  
**Visualization:** Michael Pimentel-Galvan,  
Jonathan L. Payne  
**Writing – original draft:** Michael  
Pimentel-Galvan  
**Writing – review & editing:** Kimberly  
V. Lau, Katharine Maher, Tapan Mukerji,  
Daniel J. Lehrmann, Demir Altiner,  
Jonathan L. Payne

which ongoing anoxia and greenhouse climate may have inhibited Early Triassic recovery of marine ecosystems (Hallam, 1991; Lau et al., 2016; Romano et al., 2013; Sun et al., 2012; Zhang, Algeo, et al., 2018). Testing such predictions requires data on extinction and recovery patterns as well as quantitative interpretation of geochemical proxies for ocean oxygenation and paleoclimate to guide Earth system models.

The most important paleo-redox proxy for constraining changes in global ocean oxygenation across the Permian-Triassic (P/Tr) transition is the uranium isotope ratio. Uranium is a redox-sensitive element with distinct isotope ratios between oxidized and reduced depositional environments due to isotope fractionation during uranium reduction (Brennecke et al., 2011; Stirling et al., 2007; Weyer et al., 2008). Under anoxic conditions, the reduction of U(VI) to U(IV) results in a decrease in uranium solubility and corresponding increase in the  $^{238}\text{U}/^{235}\text{U}$  ratio of the reduced product relative to the source fluid (Bigeleisen, 1996; Stirling et al., 2007). Increased uranium reduction near the sediment-water interface results in preferential partitioning of  $^{238}\text{U}$  into the anoxic sediments, while the residual U(VI) in the water column becomes enriched in  $^{235}\text{U}$ , imprinting seawater with a more negative  $\delta^{238}\text{U}$  signature (Andersen et al., 2014, 2017; Lau et al., 2020). The residual seawater uranium is then incorporated into carbonate sediments such that a negative excursion in the carbonate record tracks the increased partitioning of uranium into the anoxic sediments (Brennecke et al., 2011; Lau et al., 2016, 2019; Zhang, Algeo, et al., 2018, 2020). When anoxic depositional settings expand, the concentration of U, [U], becomes lower in seawater and in carbonate sediments deposited under oxygenated conditions because of the increased removal of uranium from seawater into anoxic sediments. Thus, variations in the uranium record from shallow-marine carbonates should reflect global trends in seawater [U] and  $\delta^{238}\text{U}$  because the residence time of uranium in the modern ocean (ca. 320–560 kyr) is two orders of magnitude longer than the ocean mixing time (Dunk et al., 2002). The effect of isotope fractionation during the precipitation of carbonate sediments and subsequent diagenesis must also be taken into consideration in quantitative reconstructions because diagenetic noise or systematic error will influence the precision and accuracy of data interpretation (Tissot et al., 2018; X. Chen et al., 2016, 2018).

Previous studies have compared [U] and  $\delta^{238}\text{U}$  of multiple stratigraphic sections from the end-Permian extinction interval through the Middle Triassic to reconstruct global seawater redox conditions for the Permian extinction and subsequent recovery. Brennecke et al. (2011) calculated the change in the relative magnitudes of the oxic and anoxic sinks for uranium before and after the end-Permian mass extinction using average values for the pre- and post-extinction intervals while assuming steady state during each interval, and Lau et al. (2016) used a forward model of the uranium cycle to conduct a visual comparison of model predictions to trends in their data, but neither study quantified the uncertainty of the model estimates for the extent or duration of the predicted anoxia. Furthermore, neither study systematically considered the potential influence of uncertainty in key parameters of the uranium cycle in the interpretation of uranium data. When uncertainty in the parameters used in the models (e.g., isotope fractionation during uranium reduction) is not considered, resulting interpretations of the time history of seafloor anoxia may indicate greater precision than is warranted and could even differ systematically from the true history. Recently, Monte Carlo simulations have been used to quantify uncertainties introduced by early diagenetic alteration and the  $\delta^{238}\text{U}$  of uranium input via rivers (Hülse et al., 2021; Zhang et al., 2020) and to fit data with uncertainty over longer timescales while assuming that each data point represents a steady state of the uranium cycle (Stockey et al., 2020). A Bayesian inverse approach was taken to interpret uranium isotope records across several episodes of ocean anoxia, including the end-Permian (Kipp & Tissot, 2022). No prior study has used the combined uranium isotope and concentration records to constrain the time history of marine anoxia, nor has any considered the joint posterior distributions of the uncertain parameters, which are critical for understanding how improved constraint on any one parameter may influence constraint on other parameters.

Quantifying uncertainty in the time history of ocean anoxia as well as in the values of key parameters in the uranium cycle model is essential if the extent of seafloor anoxia as indicated by proxy data is to be used to calibrate Earth system models for purposes of studying the intensity and selectivity of extinction (cf. Penn et al., 2018).

In this study, we address the challenge of quantifying uncertainty in the behavior of the uranium cycle and the extent of marine anoxia during the Permian/Triassic (P/Tr) transition and its aftermath. We use Monte Carlo simulations of the uranium cycle model to explore parameter space and select the best-fitting simulations via comparison to a global compilation of published uranium concentration and isotope data (Figure 1). The parameter values from the set of best-fitting Monte Carlo simulations provide estimates, with uncertainty, for the key parameters in the model, including the time history of seafloor anoxia.

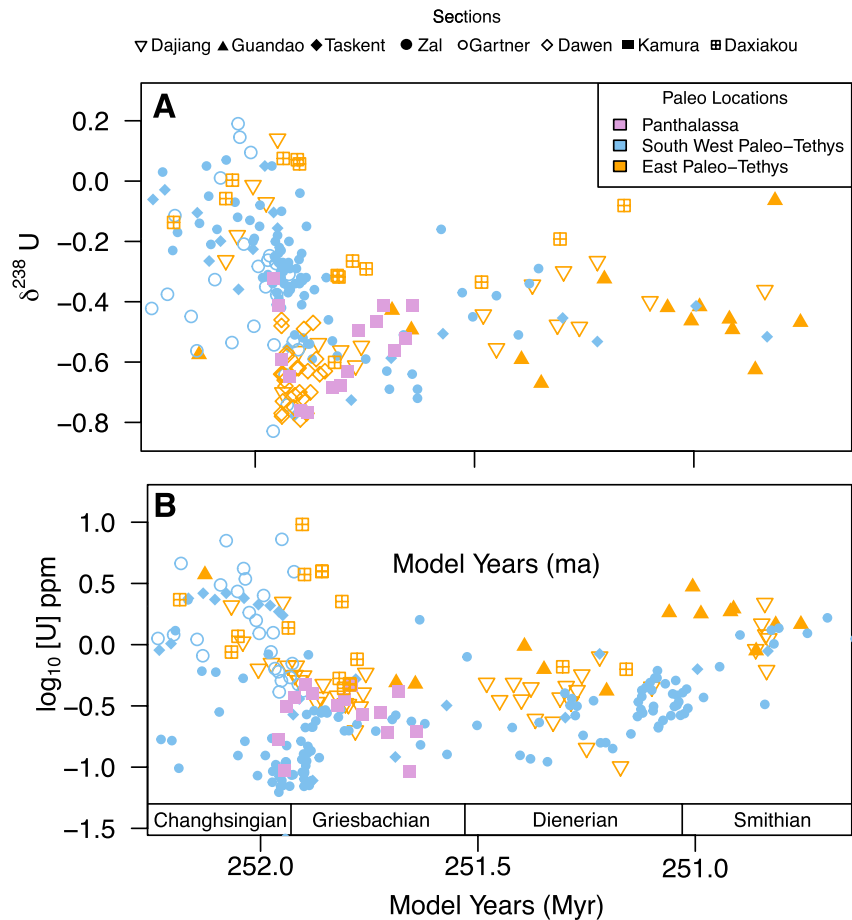


**Figure 1.** Composite uranium records illustrating coherent variation across widely distributed stratigraphic sections. (a) Uranium isotope data. (b) Uranium concentration data. Raw data and their sources are available in Table S1 in Supporting Information S1.

## 2. Data and Methods

The data set used here includes uranium concentrations and isotope ratios from carbonate rock samples spanning eight stratigraphic sections, all of which were compiled from previous studies. In total, the data set contains 292 measurements of uranium concentration and 253 measurements of uranium isotope ratio. The isotope ratio measurements were compiled and placed on a common radiometric timescale by Zhang et al. (2020). Uranium concentration values were compiled as part of this study. Uranium concentrations for samples not within the Zhang data set were added onto the common time scale. More information about the sections and samples can be found in Supporting Information S1.

Based on the combined data sets, the average  $\delta^{238}\text{U}$  composition in the Upper Permian, below the main extinction horizon, is  $-0.17\text{‰}$ , dropping abruptly to a minimum value of  $-0.83\text{‰}$  immediately above the P/Tr boundary (Figure 1). Analytical error (two standard deviations) on the isotope ratios ranges from  $0.01\text{‰}$  to  $0.23\text{‰}$ . Uranium concentrations also decrease abruptly across the P/Tr boundary, from  $\sim 3.36$  to  $\sim 0.06$  ppm. We interpret these trends to be largely representative of global changes in seawater uranium content for two reasons. First, the shallow-marine uranium records sampled from the core representing the Panthalassa Ocean (Kamura core) exhibit a similar trend (Figure 1) to records from sections sampled from the margin of Gondwana (Tashkent and Zal) and sections from the eastern Paleo-Tethys (Dajiang, Dawen, and Daxiakou). Second, the trends in  $[\text{U}]$  also agree with trends in other published records of uranium isotopes and concentrations in sedimentary rocks spanning the P/Tr boundary in Saudi Arabia, Iran, Italy, and China (Brennecke et al., 2011; Ehrenberg et al., 2008; Lau et al., 2016; Song et al., 2012; Tavakoli & Rahimpour-Bonab, 2012; Wignall & Twitchett, 1996; Wignall et al., 2010).

### 2.1. Model Calculations

Uranium isotopes and seawater concentrations were modeled using a mass-balance box model of the uranium cycle. Following Lau et al. (2016), we used coupled differential equations to describe the uranium concentration ( $[U]$ ) and isotope composition ( $\delta^{238}\text{U}$ ) of the ocean as a function of time. First, we describe the change in seawater uranium content with respect to time as the difference between the riverine input and the burial fluxes into anoxic and other sediments:

$$\frac{dU}{dt} = J_{\text{riv}} - J_{\text{anox}} - J_{\text{other}} \quad (1)$$

In this equation,  $U$  is the molar uranium inventory in the ocean,  $J_{\text{riv}}$  is the input source consisting of the modern-day riverine flux ( $0.4 \times 10^8$  mol U/y),  $J_{\text{anox}}$  is the removal of uranium from seawater via burial in anoxic sediment and  $J_{\text{other}}$  is the sum of any other sinks, including those associated with ferruginous and suboxic sediments. We chose not to model ferruginous and suboxic sinks because the uncertainty associated with these sinks is large, and there are interrelationships between suboxic, ferruginous, and anoxic sinks that are not within the scope of this study (Cole et al., 2020; Gilleaude et al., 2019; Stockey et al., 2020).  $J_{\text{anox}}$  and  $J_{\text{other}}$  can be further defined as:

$$J_{\text{anox}} = k_{\text{anox}} \times f_{\text{anox}} \times U \quad (2)$$

$$J_{\text{other}} = k_{\text{other}} \times (1 - f_{\text{anox}}) \times U \quad (3)$$

where  $k_{\text{anox}}$  and  $k_{\text{other}}$  are rate constants calculated from the modern uranium system, and  $f_{\text{anox}}$  is the fraction of seafloor impacted by bottom-water anoxia. Uranium concentration was determined by dividing the molar inventory of uranium by the volume of seawater, assumed to be equivalent to the modern volume of  $1.414 \times 10^{21}$  L.

Second, we describe the change in the uranium isotope composition of seawater with respect to time:

$$\frac{d\delta_{\text{ocean}}}{dt} = \frac{J_{\text{riv}} \times (\delta_{\text{riv}} - \delta_{\text{ocean}}) - J_{\text{anox}} \times \Delta_a - J_{\text{other}} \times \Delta_o}{U} \quad (4)$$

The model assumes continental  $\delta_{\text{riv}}$  of  $-0.3\text{‰}$  (Tissot & Dauphas, 2015). Here,  $\delta_{\text{ocean}}$  is the  $\delta^{238}\text{U}$  value of seawater.  $\Delta_a$  is the effective isotope fractionation factor (isotope offset) associated with anoxic sediment deposition, and  $\Delta_o$  is the isotope fractionation factor associated with the other sinks. Any early diagenetic effects are indirectly incorporated into  $\Delta_o$  because they occur when the carbonate sediment is still in contact with seawater-derived fluids.

### 2.2. Solving the Coupled Models

Both equations are solved using an ordinary differential equation solver function, `lsoda`, within the “deSolve” package (v033. i09; Soetaert et al., 2010) in R (v4.0.3; R Core Team, 2020), which switches automatically between non-stiff (Adams) and stiff (dense or banded Jacobian) methods as required. The initial condition for the isotope model was the average value of the sample  $\delta^{238}\text{U}$  data below the P/Tr boundary, while the initial condition for the concentration model was based on Morford and Emerson (1999), a study that used a diagenesis model and global estimates of organic carbon rain rate along with bottom-water oxygen concentrations to determine the sensitivity of trace metals such as uranium in sediments in the modern ocean. The other parameters are either constants or are allowed to vary across Monte Carlo simulations (Tables S2 and S3 in Supporting Information S1). Two of these parameters, duration and extent of anoxia, are the outcomes of interest because the primary goal of the study is to constrain the time history of ocean anoxia and its associated uncertainty given current data. The two models are coupled via the shared forcing from the time history of seafloor anoxia.

### 2.3. Setting up the Monte Carlo Simulations

We used Monte Carlo simulations to explore the model space under a variety of scenarios involving forcing by changes in the extent of marine anoxia as a function of time. We simultaneously treat the effective isotope fractionation factor associated with anoxia,  $\Delta_a$ , as uncertain to obtain empirical constraint on its values.

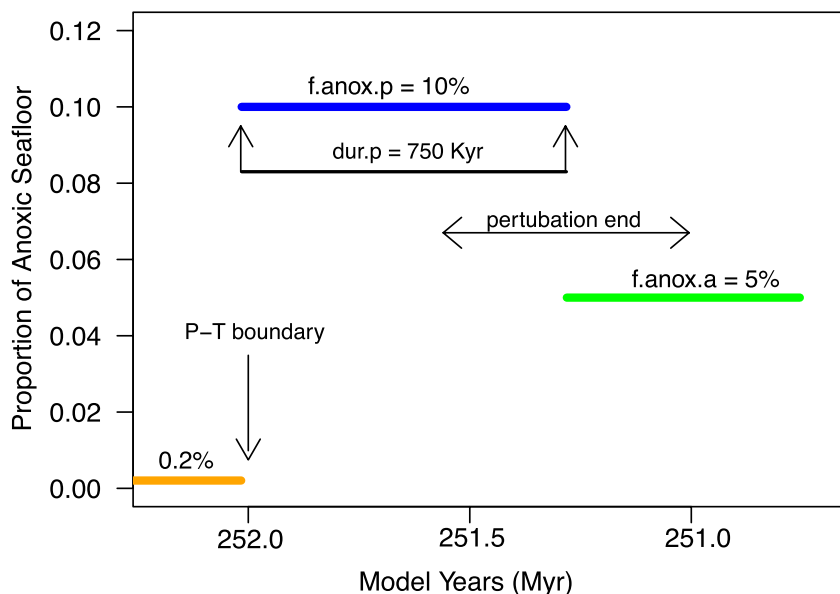


**Figure 2.** Model design, illustrating the use of three intervals with different extents of anoxia to force the uranium cycle. The initial pre-boundary interval uses a constant amount of anoxia based on the modern value of 0.2%. The second interval ( $f_{anox,p}$ ) right after the P/Tr boundary varies in duration and intensity for each model run. This example displays a model run that experiences an initial 750 kyr interval of 10% anoxia ( $f_{anox,p}$ ), followed by 5% anoxia for the remainder of the model run ( $f_{anox,a}$ ).

#### 2.4. Parameters of Interest

The parameters that we allow to vary in the Monte Carlo simulations determine the duration and intensity of seafloor anoxia as well as its impact on the uranium isotope composition of seawater via the fractionation associated with anoxic sinks. These parameters can be grouped together based on whether they affect the model forcing or determine its response to the forcing. The model is forced using a three-step approach (Figure 2) where anoxia begins at a low value similar to the modern ocean and then increases via a step function at the time of the end-Permian mass extinction to an initial post-extinction value ( $f_{anox,p}$ ) and then is allowed to change again via a step to a new value ( $f_{anox,a}$ ) drawn from the same range of values as  $f_{anox,p}$  for the remainder of the model run. A three-segment approach was chosen because these simulations were designed to quantify the long-term average level of anoxia rather than to detect the potential presence of multiple, short-lived perturbations during the recovery period. Further work using an increased number of model segments or more episodic perturbations (Zhang, Algeo, et al., 2018) could help further constrain the parameters but add substantially to the model space that must be explored and may require greater data density to yield meaningful results.

Uniform priors were used for all parameters explored. The bounds of the priors for  $f_{anox,p}$  and  $f_{anox,a}$  were 0.0 and 0.7 to ensure that the Monte Carlo simulations explored all plausible extents of anoxia, even those beyond the extents inferred in previous studies (cf. Lau et al., 2016; Penn et al., 2018). The duration of the initial interval of anoxia ( $dur_p$ ), which is the amount of time each model experiences  $f_{anox,p}$ , was allowed to vary between 0 and 1.7 Myr (the maximum possible given the duration of the model runs). The fraction of seafloor anoxia was then set to  $f_{anox,a}$  for the remainder of the model run.

The parameters that determine the model's response to the forcing from anoxia are the effective fractionation factor,  $\Delta_a$ , and the carbonate diagenetic offset,  $dia$ , applied to the output isotope ratios. The fractionation factor within an anoxic environment,  $\Delta_a$ , was allowed to vary between 0.0‰ and 1.2‰ based on the potential range of effective fractionation factors (Andersen et al., 2014). The diagenetic offset associated with carbonate diagenesis,  $dia$ , addresses later diagenesis not incorporated into the model due to the lack of contact with seawater. For each model,  $dia$  was chosen from a normal distribution with a mean of +0.24‰ and standard deviation of 0.06‰ (Romaniello et al., 2013; Tissot et al., 2018; X. Chen et al., 2018).

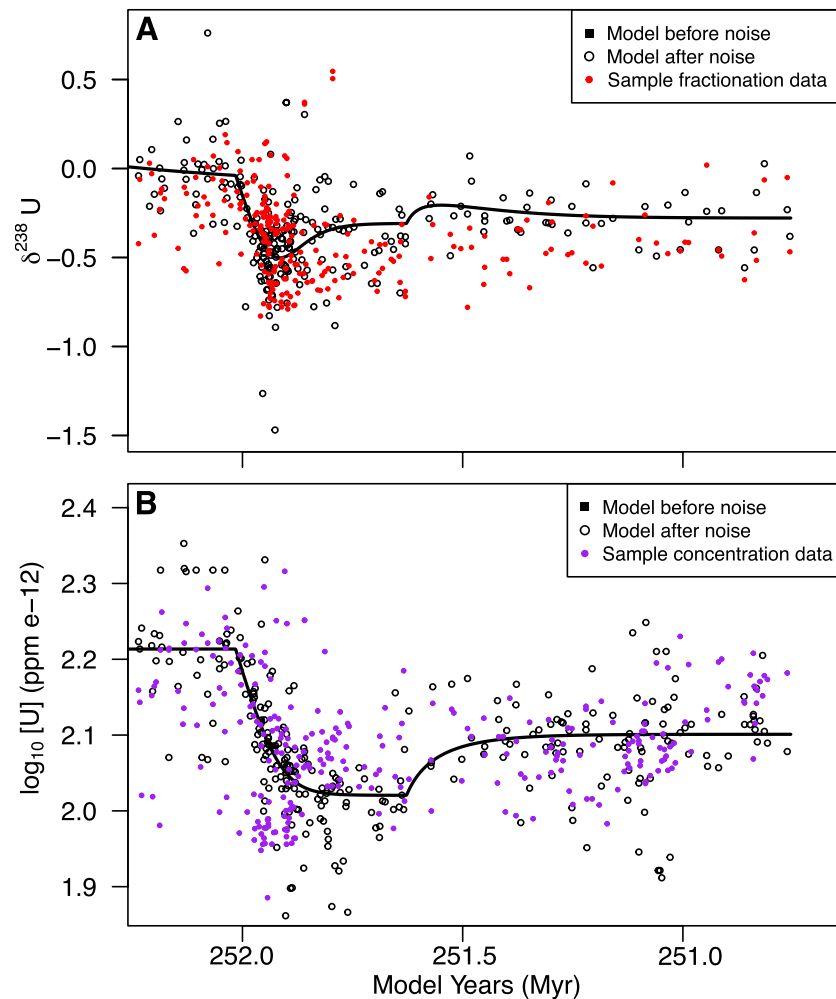


**Figure 3.** Example of model output for one Monte Carlo simulation versus measured data. The measured data are illustrated using colored closed circles, red in panel (a) referring to measured  $\delta^{238}\text{U}$  and purple in panel (b) referring to measured  $[\text{U}]$ . The deterministic model output is depicted using a black curved line, and model output with added noise for time steps corresponding to measured data are depicted using open circles. (a) Isotope data and model output. (b) Uranium concentration data and model output.

### 2.5. Model Data Comparison

We conducted 25,000 Monte Carlo simulations of the uranium cycle. The simulated data were then compared to the real data to find the model runs whose output most closely resembled the measured values of uranium concentrations and isotope ratios. The parameters used to create the best-fitting models provide posterior distributions, and therefore measures of uncertainty on the values of those parameters. Each iteration of the model generates simulated concentration and isotope ratios for every 1,000-year time step.

First, the simulated values that correspond to the ages of measured (i.e., real) data were extracted for the model-data comparison. Because the models are deterministic whereas the data contain noise, a further step for creating a realistic comparison between model output and measured data is to add noise to the extracted simulated data with a similar distribution to that in the sample data (Figures 3a and 3b). The distribution of noise was calculated using the first differences of the measured sample data (i.e., the differences between consecutive data points). We took this approach because the sample-to-sample variation is larger than the analytical measurement error and is likely to reflect heterogeneities in the rock rather than short-term variation in the global uranium cycle, given the long residence time of uranium in seawater (>100 kyr) relative to the age differences between consecutive samples (mean:  $\sim 7$  kyr). Therefore, we treat the rock heterogeneity as the more important source of noise in the

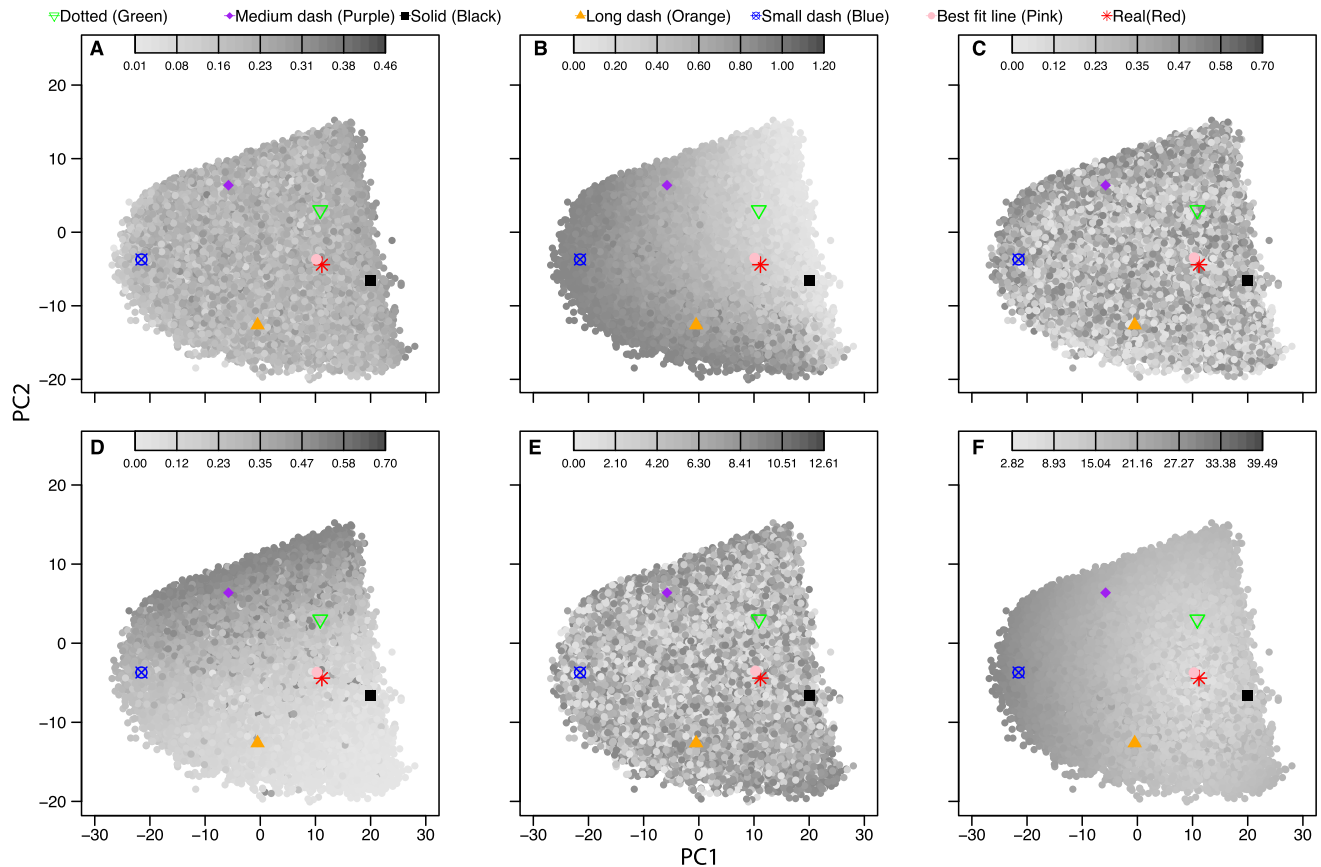


**Figure 4.** Plots of Monte Carlo simulations versus measured data in principal component analysis (PCA) space. Each Monte Carlo simulation is illustrated as a single point in this plot of PC1 versus PC2 and the real data are illustrated as a red asterisk. Selected model runs are illustrated as colored symbols and their forcing and predictions for  $\delta^{238}\text{U}$  and  $[\text{U}]$  illustrated in Figure 5. In each panel, the shading of the model runs is based on the value of a specific model parameter. (a) *dia*, (b)  $D_{\text{anox}}$ , (c)  $f_{\text{anox},a}$ , (d)  $f_{\text{anox},p}$ , (e) *dur.p*, and (f) distance from measured data in PCA space.

data for the purposes of the model and the sample-to-sample variation as the most useful approximation of that noise, in contrast with other efforts to invert uranium isotope records (Kipp & Tissot, 2022). The variance of the measured isotope sample data is 0.052‰. A variable carbonate diagenetic isotope offset, *dia*, was added back to the model output to account for diagenesis after initial seawater contact to produce modeled carbonate  $\delta^{238}\text{U}$  data that was compared with measured sample data. The model output of seawater concentrations was adjusted to predict concentrations in carbonate rocks using a partition coefficient of 1.4 (Maher et al., 2006), assuming most of the carbonate sediment was originally aragonitic (Stanley et al., 1999). The concentration data were  $\log_{10}$ -scaled to address the strong right skew in the data for purposes of model-data comparison; the log-scaled variance is 0.137. This approach may overestimate the noise in the data because some of the sample-to-sample change is related to the true signal, but as the data points become arbitrarily close to one another, the first differences will converge on the noise in the data.

Monte Carlo simulation output was compared to measured data by assessing the distance between model runs and measured data in principal component analysis (PCA) space. To achieve this comparison, matrices were created for both the simulated concentration and isotope ratio output at the time horizons corresponding to the measured data. The corresponding measured data were then added as the final column to each matrix. The matrices were then standardized to unit variance to be used in the PCA so that differences in scale between concentrations and isotope ratios did not cause one to influence the PCA more than the other. Finally, the two data frames were bound together and subjected to PCA.

Distance in PCA space provides a measure of similarity in outcome, enabling comparison among Monte Carlo simulations and of the measured data to each simulation (Figure 4). Distances between model runs and measured

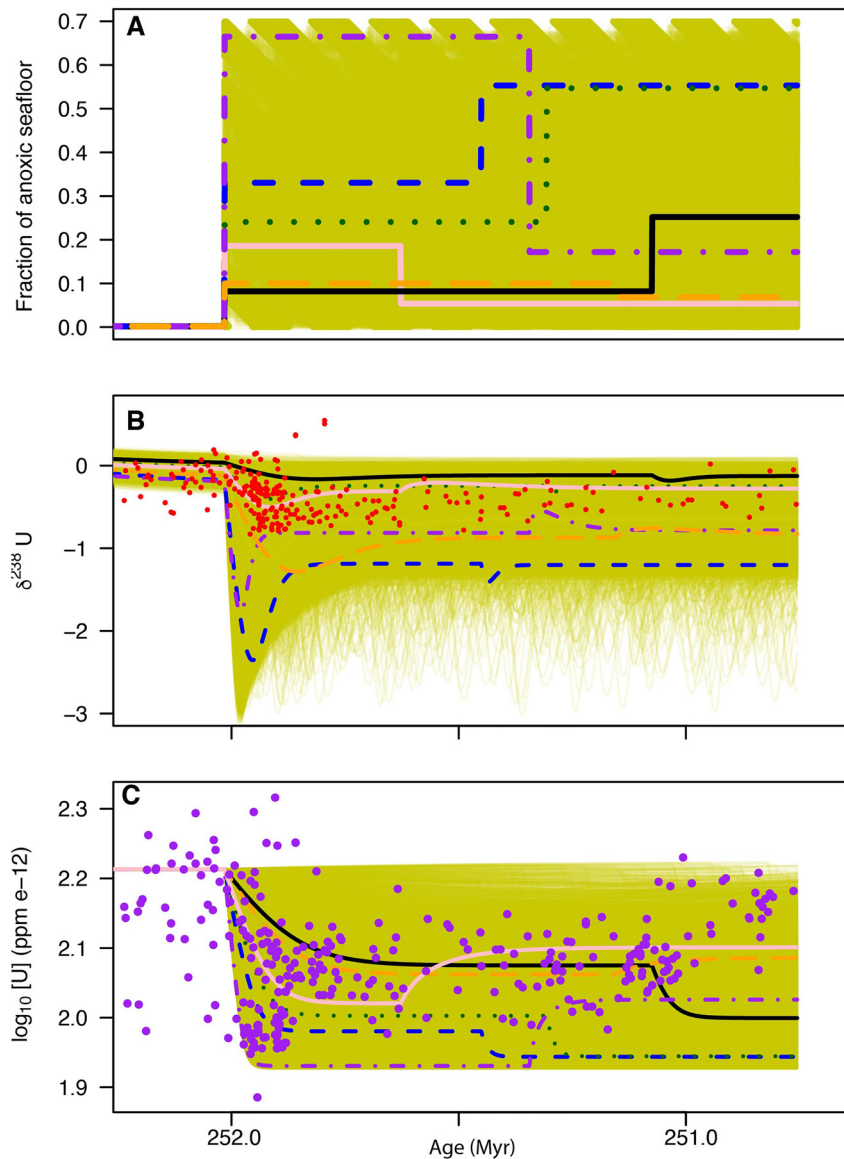


**Figure 5.** Forcing and output from Monte Carlo simulations plotted as a function of age, illustrating the range of model output. Each simulation is plotted as a gold curve. Selected simulations are plotted in thicker, colored lines and correspond to selected simulations highlighted in Figure 4 to illustrate the correspondence between model predictions and principal component analysis space. The fraction of anoxic seafloor used to create each individual model run is depicted in (a). Measured data are illustrated as red dots for isotope ratios (b) and purple dots for concentrations (c).

data were calculated using all PCA axes that explained more than 1% of the variance, which were the first six axes in this case (Figure 5). Using the Approximate Bayes Computation (ABC), the distance of each individual simulation from the measured data in the six-dimensional PCA space was calculated and the simulations that most closely resemble the observed data were identified. ABC methods allow a broad range of models to be considered for statistical inference (Sunnåker et al., 2013). The calculated distance of each model was used to find the top 1% of models that most closely resemble the measured data (Figure 6). The parameter values from these best-fitting models provide approximate posterior distributions for the parameters of interest (Figure 7). This PCA approach differs from other Bayesian inverse model approaches because it not only compares each model against the sample data but also against every other simulation, allowing us to rank and find the best-fitting simulations and corresponding parameters used to create those simulations. The code used is available at <https://purl.stanford.edu/qd321fz3803>.

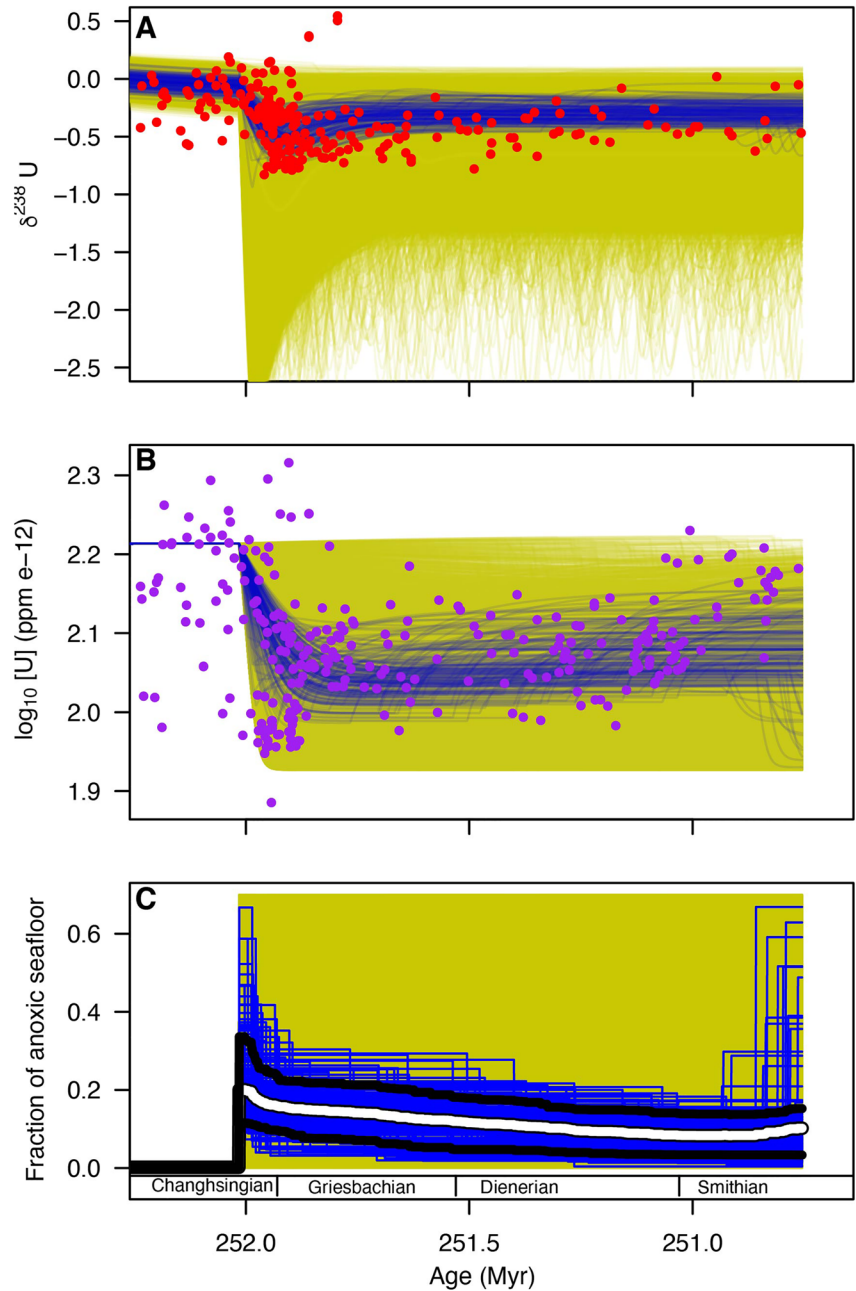


**Figure 6.** Comparison between Monte Carlo simulations and model data, highlighting the best-fitting 1% of simulations based on distance from measured data in principal component analysis space. (a) Uranium isotopes. (b) Uranium concentrations. (c) Extent of seafloor anoxia. Total simulations in yellow, best-fitting simulations in blue. White line indicates the average forcing across the best-fitting models for each time step while black lines are the 10th and 90th quantiles of the best-fitting models.

### 3. Results

#### 3.1. Model Output

The Monte Carlo simulation output spans the range of the observed data, with only a few exceptions, and includes isotope ratios and concentrations beyond the range observed (Figures 6a and 6b). This overlap between the observed data and the output from the Monte Carlo simulations is also apparent in PCA space, where the observed data fall well within the range of the simulations along the first two principal component axes, which together

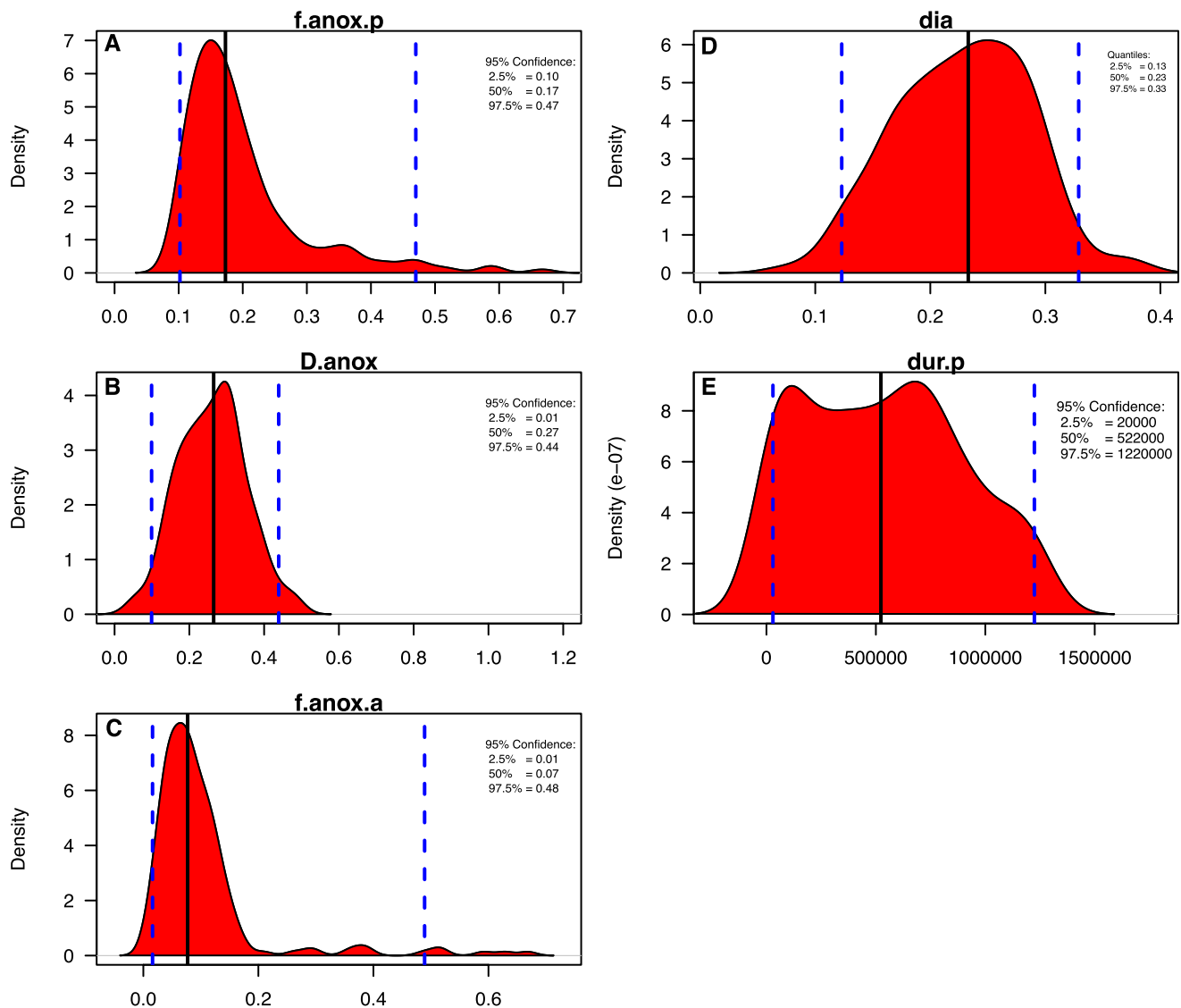


**Figure 7.** Posterior distributions for model forcing and other parameters based on the best-fitting 1% of Monte Carlo simulations. (a) Extent of anoxia during the initial perturbation. (b) Effective fractionation factor for uranium deposition in anoxia environments. (c) Extent of anoxia during the remainder of the model run, after the initial perturbation. (d) Diagenetic offset of isotope data in carbonates from initial value. (e) Duration of the initial perturbation. Medians are illustrated as vertical black lines and the middle 95% of the distribution is bounded by dashed blue lines.

account for 55.3% of the variation in the total PCA space (Figure S1 in Supporting Information S1). This overlap between simulated and measured data indicates that the parameter distributions from the model runs most closely resembling the measured data are potentially informative about the conditions that generated the measured data.

## 4. Discussion

### 4.1. Best Fit Parameters Values

The posterior distributions for the parameters allowed to vary within the Monte Carlo simulations are substantially narrower than the priors (Figure 7). The median of the posterior distribution for extent anoxia during the perturbation ( $f_{anox.p}$ ) is 0.18 (95% CI: [0.11, 0.48]; Figure 7a) and the median of the posterior distribution for extent anoxia after the perturbation ( $f_{anox.a}$ ) is 0.07 (95% CI: [0.01, 0.54]; Figure 7c). The median of the posterior distribution for the duration of the perturbation is 520 kyr (95% CI [20 kyr, 1.2 Myr]; Figure 7e). The median of the posterior distribution for the fractionation factor associated with anoxic sinks ( $\Delta_a$ ), is 0.27‰ (95% CI: [0.18,

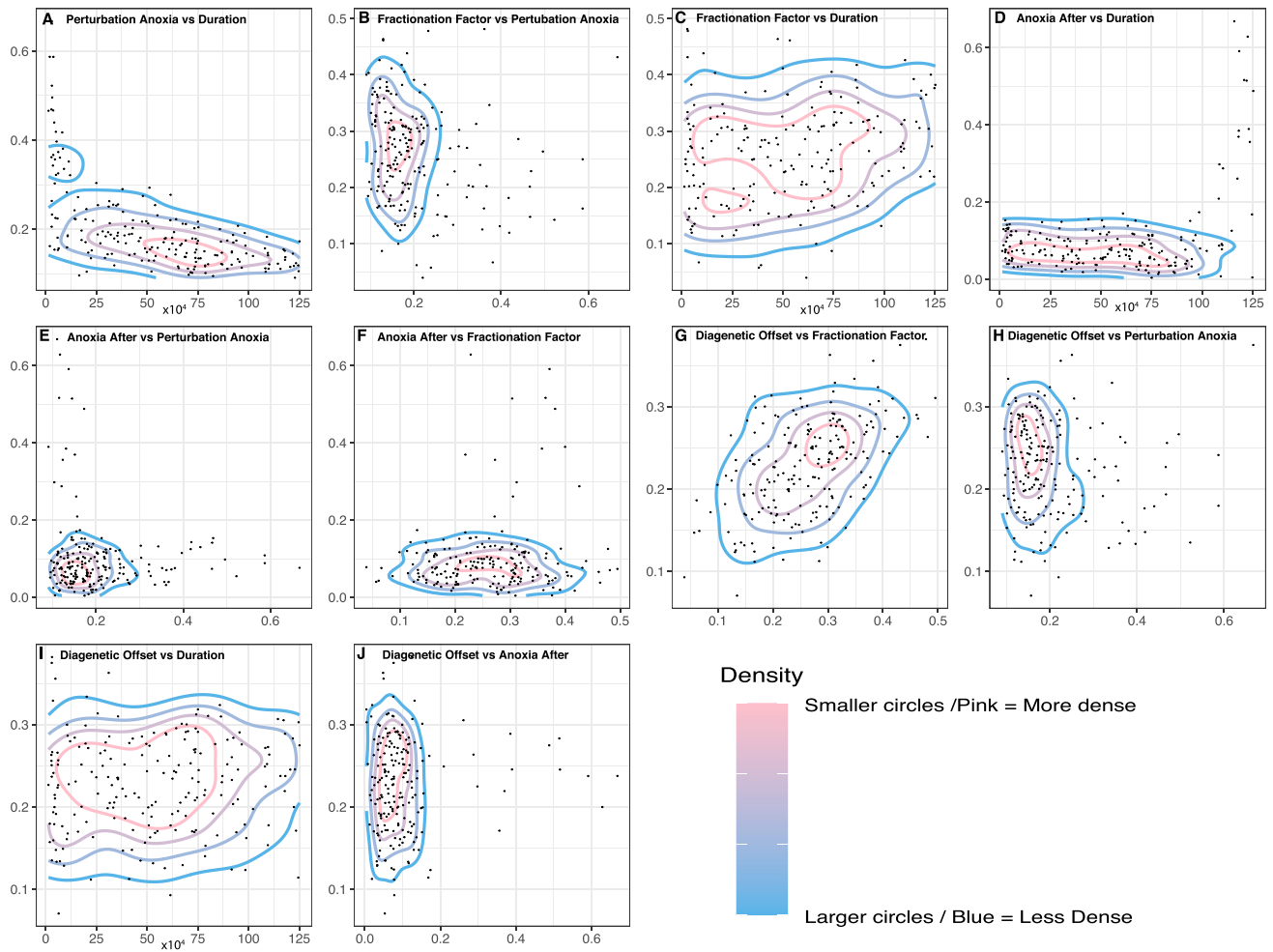


**Figure 8.** Scatterplots of model parameters in the posterior distributions (Figure 7), illustrating the covariation between the best fit parameters. (a) Perturbation anoxia vs Duration. (b) Fractionation Factor vs Perturbation Anoxia. (c) Fractionation Factor vs Duration. (d) Anoxia after perturbation vs Duration. (e) Anoxia after perturbation vs Perturbation anoxia. (f) Anoxia after perturbation vs Fractionation Factor. (g) Diagenetic offset vs Fractionation factor. (h) Diagenetic offset vs Perturbation Anoxia. (i) Diagenetic offset vs Duration. (j) Diagenetic offset vs Anoxia after perturbation.

0.44; Figure 7b). The best-fitting simulations did not narrow the prior for the diagenetic offset, *dia* (Figure 7d). The best-fitting simulations have anoxia that ranges from a mean of  $18\% \pm 4\%$  (Figure 6c) of seafloor area at the extinction boundary ( $f_{anox,p}$ ) and it steadily decreases to around  $15\% \pm 4\%$  (Figure 7c) over the span of  $\sim 850$  kyr (Figure 6c). However, toward the end of the model simulation ( $>1.2$  Myr) a few of the best-fitting models exhibit increases in anoxia ( $>20\%$ ). In the best-fitting models, anoxia remained between 1% and 50% (Figure 7e) of seafloor area after the initial perturbation subsided. The duration of the perturbation for the best-fitting models ranges from 20 kyr to 1.2 Myr (Figure 7d). The best-fitting model runs with short perturbation durations are also associated with greater extents of anoxia during the perturbation ( $>20\%$  seafloor area) (Figure 8a) whereas model runs with longer initial perturbation durations are associated with lesser extents of anoxia ( $<20\%$  seafloor area) (Figure 8a). This correlation between intensity and duration of anoxia in the posterior distributions indicates that improved constraint on either the intensity or the duration of Early Triassic anoxia will also, indirectly, improve constraint on the other parameter.

#### 4.2. Parameter Comparison

Because the uranium concentration and isotope composition of seawater are impacted both by the intensity and duration of anoxia, there is reason to expect that the posterior distributions of some or all parameters are not independent. Indeed, the posterior distributions for the duration and extent of anoxia forced during the perturbation

( $f_{anox,p}$ ) exhibit a strong inverse correlation (Figure 8a, Spearman's rho:  $-0.66$ ,  $p = 2.2 \times 10^{-16}$ ) when the duration of the initial perturbation is shorter than 100 kyr and weakens after the perturbation. The intensity of the initial interval of anoxia ( $f_{anox,p}$ ) exhibits a weak inverse correlation with the isotope fractionation in anoxic environments ( $\Delta_a$ ) (Figure 8b, Spearman's rho:  $-0.19$ ,  $p = 0.005$ ). Because  $\Delta_a$  is the effective fractionation factor associated with anoxic sediment reduction, less intense levels of anoxia are required to produce model runs that similarly follow the measured data when  $\Delta_a$  is large.

### 4.3. Assessing the Uranium Isotope and Concentration Data Individually

To assess whether the overall model fit represents a compromise between differing signals from the concentration and isotope ratio data versus reflecting a common signal in both data types, we conducted the same model-data comparison described above for each data type separately. This analysis began with the same Monte Carlo simulation output used for the full analysis described above. Using the isotope data alone, the best-fitting models on average do not capture the abrupt negative excursion at the beginning of the perturbation (Figure 9). Comparing the posterior distributions of the simulations using isotope data only (Figure 10) to the posteriors of both isotope and concentration data together (Figure 7), the isotope-only posteriors are shifted toward less intense anoxia during the perturbation ( $f_{anox,p}$  5.1%–25%) but more intense anoxia during the interval afterward ( $f_{anox,a}$  1%–67%). It also indicates higher values of  $\Delta_a$  (0.13–0.46) and slightly lower values of diagenetic offset (0.09–0.27) (Figure 10). The posterior distributions derived from comparison to concentration-only results (Figures 11 and 12) have a more limited range of values for the duration of the perturbation (54–750 kyr) and indicate less intense anoxia after the perturbation ( $f_{anox,a}$  2%–11%) compared to the full analysis; however, they return a wider range of values, most of them high, for the extent anoxia during the perturbation ( $f_{anox,p}$  14%–64%). This analysis also returns a wide range of effective fractionation factors, similar to the prior ( $\Delta_a$  0.05–1.17) because this model-data comparison contains no constraint from data regarding isotope ratios.

In general, for the long-term amount of anoxia, the analyses using isotopes and concentrations separately agree in requiring a large increase in anoxia at the P/Tr boundary and the persistence of extensive anoxia across the remainder of the study interval. There are also minor differences. For example, the concentration-only results tend to indicate a more severe and short-lived onset of anoxia whereas the isotope data are better fit by models that imply a less severe but longer-lasting interval of anoxia at the P/Tr boundary. Part of the reason for this difference in interpretation between the isotope-only and concentration-only results may be a greater amount of noise in the isotope data across the boundary when compared to the concentration data. Another potential source of discrepancy is systematic variation across time in the proportion of aragonite versus calcite in the original sediments, which would violate the assumption of a constant distribution coefficient describing the relationship between the concentration of uranium in seawater and carbonate sediments.

## 5. Conclusion

### 5.1. Duration and Intensity

The posterior distributions of the best-fitting simulations overlap the conditions modeled by Lau et al. (2016) based on visual comparison to data, which assumed 20% seafloor anoxia for 30 kyr followed by 5% seafloor anoxia for the remainder of the modeled interval (1.7 Myr) and are also consistent with earlier calculations by Brennecke et al. (2011) that suggest substantial anoxia for at least the first 50 kyr after the P/Tr boundary. The results also overlap the less extensive (10% of seafloor) anoxia calculated by Kipp and Tissot (2022). This study differs from Kipp and Tissot (2022) in a few ways, including a longer study interval, inclusion of data from more samples and sections, and consideration of uranium concentrations as well as isotope ratios in model-data comparison. The isotope-only analysis in this study yields a median posterior value of 11% seafloor anoxia, in close agreement with the result from Kipp and Tissot (2022) under the most comparable data treatment. Our overall model-data comparison indicates  $18\% \pm 4\%$  seafloor anoxia immediately following the P/Tr boundary (Figure 6c). Based on the running average of the best-fitting models, the extent of anoxia decreased to  $15\% \pm 4\%$  over a span of 800 kyr and remained in this range until the end of the study interval, with similar uncertainty. These quantitative constraints from modeling the uranium cycle are also in broad agreement with evidence from redox-sensitive proxies such as U/Th ratios and element-enrichment factors (for U, Cr, V, Co, and Ni), which

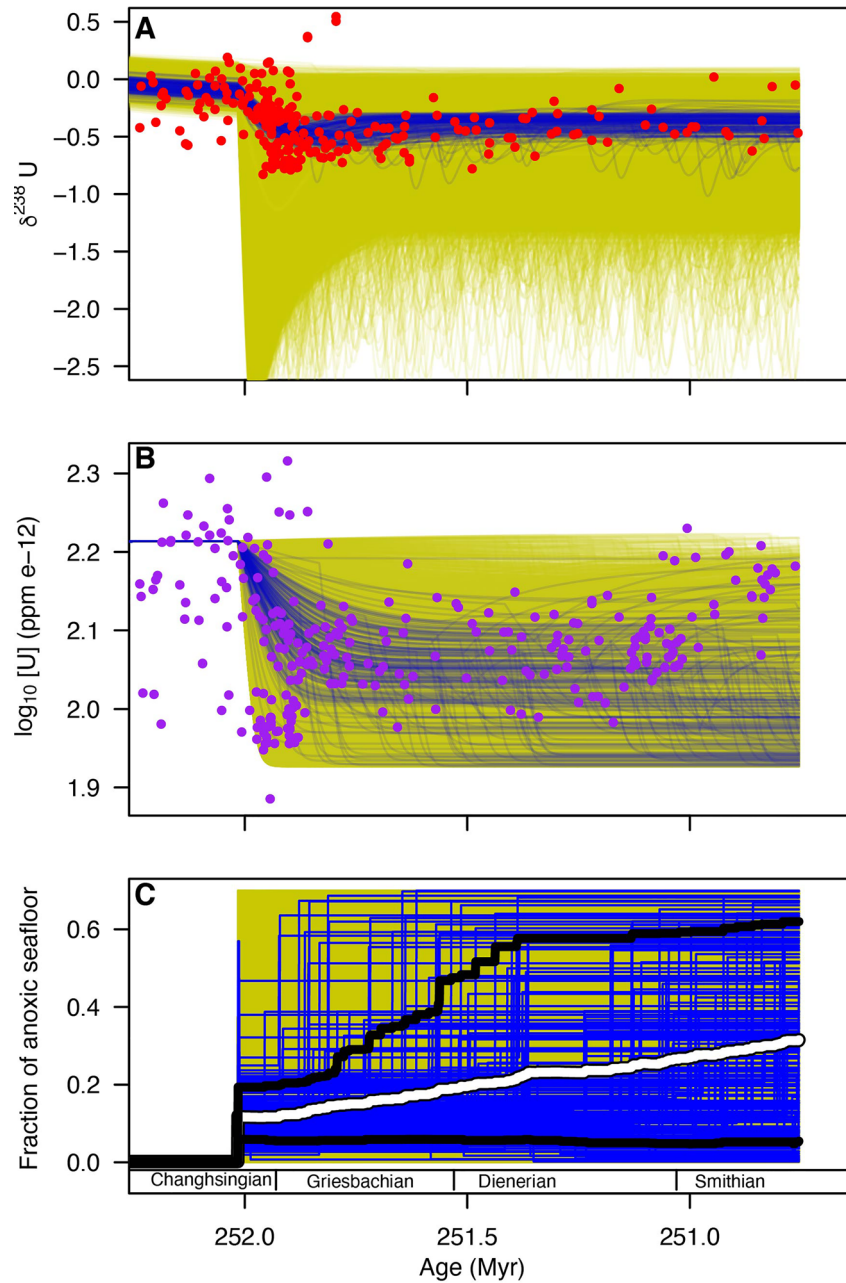


**Figure 9.** Comparison between Monte Carlo simulations and model data, using only isotope values for model-data comparison. (a) Uranium isotopes. (b) Uranium concentrations. (c) Extent of seafloor anoxia. Total simulations in yellow, best-fitting simulations in blue. White line indicates the average forcing across the best-fitting models for each time step while black lines are the 10th and 90th quantiles of the best-fitting models.

suggest a 60-kyr-long episode of intense anoxia beginning at the P/Tr boundary followed by still-expanded anoxia for at least another 450 kyr (Rampino et al., 2020).

Quantitative modeling of the uranium cycle adds to the evidence that Early Triassic anoxia persisted for well more than 1 million years, consistent with qualitative evidence from other systems, such as Th/U ratios (Wignall & Twitchett, 1996), marine fossil assemblages (Loriga et al., 1986; Z. Chen & Benton, 2012), sulfur isotopes (Bernasconi et al., 2017; Zhang et al., 2017), and the color and mineralogy of deep-sea sediments (Isozaki, 1997). This evidence agrees with the model results (Figure 7), in which intervals of intense (~20% seafloor area) anoxic perturbation lasting up to 1.2 Myr best fit the trend of both uranium isotope and concentration data. In the future,

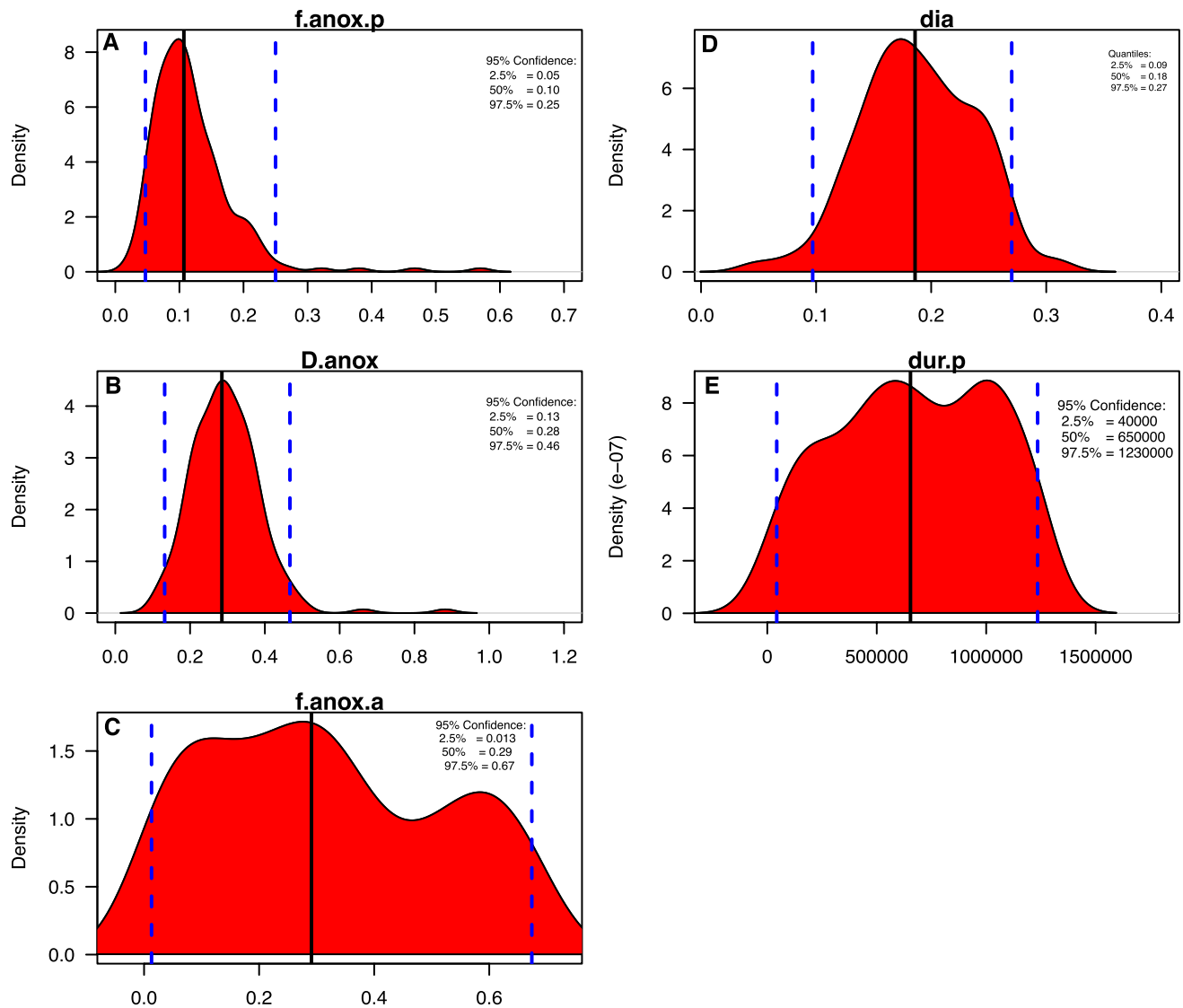


**Figure 10.** Posterior distributions for model forcing and other parameters based on the best-fitting 1% of Monte Carlo simulations using only isotope data for model-data comparison. (a) Extent of anoxia during the initial perturbation. (b) Effective fractionation factor for uranium deposition in anoxia environments. (c) Extent of anoxia during the remainder of the model run, after the initial perturbation. (d) Diagenetic offset of isotope data in carbonates from initial value. (e) Duration of the initial perturbation. Medians are illustrated as vertical black lines and the middle 95% of the distribution is bounded by dashed blue lines.

numerical models coupling forcing from seafloor anoxia to predictions for other isotope ratios and elemental concentrations could be used to expand the model-data comparison conducted in this study.

Model-data comparison indicates that expanded seafloor anoxia persisted for substantially longer than the interval modeled in this study. Anoxia was generally high even at the end of the study interval and uranium concentrations and isotope ratios remain depleted through much of the Lower Triassic (Lau et al., 2016; Zhang, Algeo, et al., 2018). Sulfur isotope ratios in evaporites also continue to trend more positively beyond the interval modeled within this study (Bernasconi et al., 2017), consistent with an ongoing interval of extensive sulfate reduction and pyrite burial. The simulations indicate, on average, a decreased level of anoxia toward the end of the modeled interval (~15%) when compared to the average perturbation anoxia (~20%) (Figure 6c), both of which are substantially higher than the pre-extinction and modern-day levels of seafloor anoxia (~0.2%).

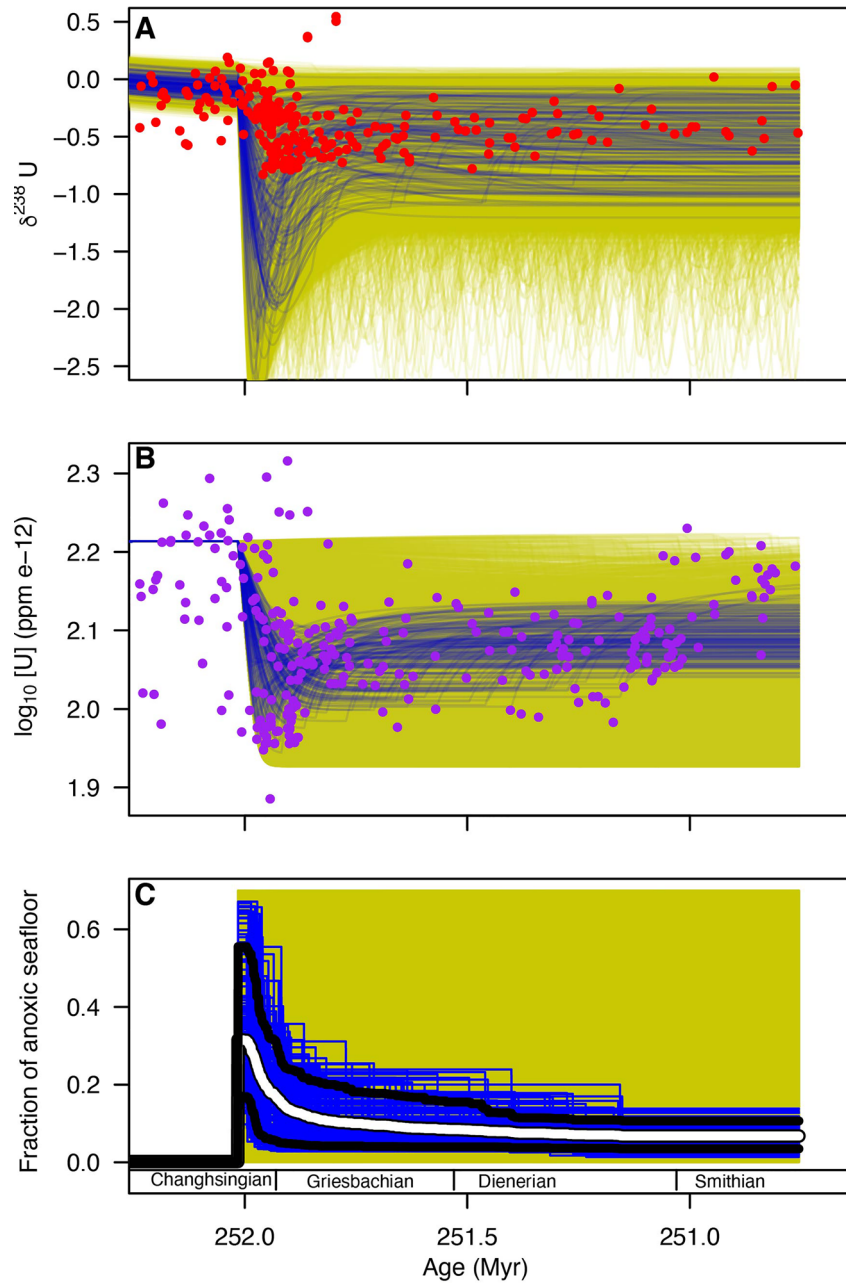


**Figure 11.** Comparison between Monte Carlo simulations and model data, using only concentration data for model-data comparison. (a) Uranium isotopes. (b) Uranium concentrations. (c) Extent of seafloor anoxia. Total simulations in yellow, best-fitting simulations in blue. White line indicates the average forcing across the best-fitting models for each time step while black lines are the 10th and 90th quantiles of the best-fitting models.

## 5.2. Implications for Biology

Model-data comparison confirms the link between intense marine anoxia and mass extinction. The extinction event was associated with the interval of most severe anoxia,  $18\% \pm 4\%$  (Figure 6c). Although the initial peak of anoxia was potentially short-lived, its extreme intensity and probable duration of more than 20 kyr helps to account for the biological devastation that resulted. This estimate is lower than the 40% seafloor anoxia produced in the general circulation model of Penn et al. (2018), but the model-data comparison in this study, which only allowed for two intervals with different levels of anoxia across 1.7 Myr in each model run, was designed to detect long-term changes and so may underestimate the initial, peak anoxia. By contrast, the Penn et al. (2018) study

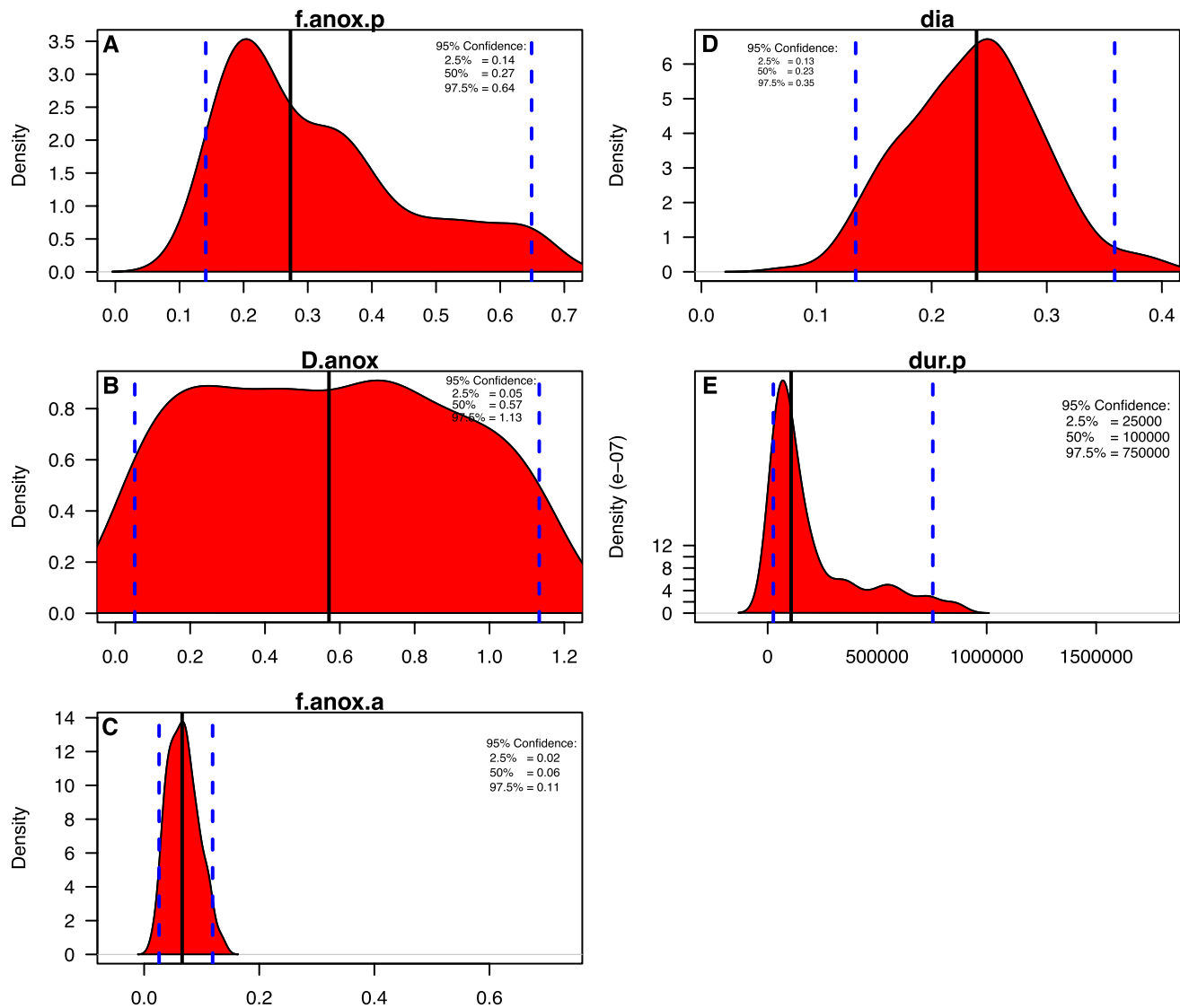


**Figure 12.** Posterior distributions for model forcing and other parameters based on the best-fitting 1% of Monte Carlo simulations using only concentration data for model-data comparison. (a) Extent of anoxia during the initial perturbation. (b) Effective fractionation factor for uranium deposition in anoxia environments. (c) Extent of anoxia during the remainder of the model run, after the initial perturbation. (d) Diagenetic offset of isotope data in carbonates from initial value. (e) Duration of the initial perturbation. Medians are illustrated as vertical black lines and the middle 95% of the distribution is bounded by dashed blue lines.

modeled only a few thousand years with the goal of capturing the impact of the peak environmental disturbance on thousand-year timescales. For the same reasons, uranium data would be unlikely to capture the short-lived oxygenation event near the P/Tr boundary indicated by thallium isotope data (Newby et al., 2021). Precisely quantifying the extent of anoxia during a short-lived peak that lasted only thousands of years would be limited by the response time of the uranium cycle (Kipp & Tissot, 2022). Ideally, one would apply a paleoredox proxy with a shorter response time than that of uranium (e.g., thallium) to the problem of peak anoxia on thousand-year timescales. Regardless of the extent of disagreement, model-data comparison provides an avenue to quantify and address the uncertainty in the reconstruction of ancient ocean oxygenation in modeling biological response through animal physiology.

The persistence of extensive, albeit lower, levels of anoxia for the 1.7-Myr interval after the P/Tr boundary is consistent with evidence of delayed biotic recovery, further extinction pulses during the Early Triassic, and the persistence of low-diversity, high-dominance communities (Hallam, 1991; Sahney & Benton, 2008; Shen et al., 2011; Song et al., 2013; Wignall & Hallam, 1992). These simulations were designed to quantify the

long-term average level of anoxia rather than to detect the potential presence of multiple, short-lived perturbations during the recovery period. Expansion of the approach employed here could be used to quantify the number, timing, and extent of subsequent pulses anoxia during Early Triassic time that may have further delayed biotic recovery beyond the effects of persistent anoxia during the first 1.7 Myr following the extinction event.

### Conflict of Interest

The authors declare no conflicts of interest relevant to this study.

### Data Availability Statement

Sample data, supplementary materials, and code used to create plots and arrive at the conclusions can be obtained here: <https://purl.stanford.edu/qd321fz3803>.

### Acknowledgments

This study was supported by funding from the School of Earth, Energy, and Environmental Sciences at the Stanford University.

### References

- Andersen, M. B., Romaniello, S., Vance, D., Little, S. H., Herdman, R., & Lyons, T. W. (2014). A modern framework for the interpretation of  $^{238}\text{U}/^{235}\text{U}$  in studies of ancient ocean redox. *Earth and Planetary Science Letters*, *400*, 184–194. <https://doi.org/10.1016/j.epsl.2014.05.051>
- Andersen, M. B., Stirling, C. H., & Weyer, S. (2017). Uranium isotope fractionation. *Reviews in Mineralogy and Geochemistry*, *81*, 799–850. <https://doi.org/10.2138/rmg.2017.82.19>
- Bambach, R. K., Knoll, A. H., & Sepkoski, J. J., Jr. (2002). Anatomical and ecological constraints on Phanerozoic animal diversity in the marine realm. *Proceedings of the National Academy of Sciences of the United States of America*, *99*(10), 6854–6859. <https://doi.org/10.1073/pnas.092150999>
- Bernasconi, S. M., Meier, I., Wohlwend, S., Brack, P., Hochuli, P. A., Bläsi, H., et al. (2017). An evaporite-based high-resolution sulfur isotope record of Late Permian and Triassic seawater sulfate. *Geochimica et Cosmochimica Acta*, *204*, 331–349. <https://doi.org/10.1016/j.gca.2017.01.047>
- Bigeleisen, J. (1996). Nuclear size and shape effects in chemical reactions. Isotope chemistry of the heavy elements. *Journal of the American Chemical Society*, *118*(15), 3676–3680. <https://doi.org/10.1021/ja954076k>
- Brennecke, G. A., Herrmann, A. D., Algeo, T. J., & Anbar, A. D. (2011). Rapid expansion of oceanic anoxia immediately before the end-Permian mass extinction. *Proceedings of the National Academy of Sciences of the United States of America*, *108*, 17631–17634. <https://doi.org/10.1073/pnas.1106039108>
- Chen, X., Romaniello, S., Herrmann, A., Hardisty, D., Gill, B., & Anbar, A. D. (2018). Diagenetic effects on uranium isotope fractionation in carbonate sediments from the Bahamas. *Geochimica et Cosmochimica Acta*, *237*, 294–311. <https://doi.org/10.1016/j.gca.2018.06.026>
- Chen, X., Romaniello, S. J., Herrmann, A. D., Wasylenki, L. E., & Anbar, A. D. (2016). Uranium isotope fractionation during coprecipitation with aragonite and calcite. *Geochimica et Cosmochimica Acta*, *188*, 189–207. <https://doi.org/10.1016/j.gca.2016.05.022>
- Chen, Z., & Benton, M. (2012). The timing and pattern of biotic recovery following the end-Permian mass extinction. *Nature Geoscience*, *5*, 375–383. <https://doi.org/10.1038/ngeo1475>
- Cole, D. B., Planavsky, N. J., Longley, M., Böning, P., Wilkes, D., Wang, X., et al. (2020). Uranium isotope fractionation in non-sulfidic anoxic settings and the global uranium isotope mass balance. *Global Biogeochemical Cycles*, *34*, e2020GB006649. <https://doi.org/10.1029/2020GB006649>
- Dunk, R., Mills, R., & Jenkins, W. (2002). A reevaluation of the oceanic uranium budget for the Holocene. *Chemical Geology*, *190*, 45–67. [https://doi.org/10.1016/S0009-2541\(02\)00110-9](https://doi.org/10.1016/S0009-2541(02)00110-9)
- Ehrenberg, S. H., Sváná, T. A., & Swart, P. K. (2008). Uranium depletion across the Permian-Triassic boundary in Middle East carbonates. *Signature of oceanic anoxia: American Association of Petroleum Geologists Bulletin*, *92*, 691–707. <https://doi.org/10.1306/02140807095>
- Gilleaudeau, G. J., Romaniello, S., Luo, G., Kaufman, A., Zhang, F., Klaebe, R., et al. (2019). Uranium isotope evidence for limited euxinia in mid-Proterozoic oceans. *Earth and Planetary Science Letters*, *521*, 150–157. <https://doi.org/10.1016/j.epsl.2019.06.012>
- Hallam, A. (1991). Why was there a delayed radiation after the end-Palaeozoic extinctions? *Historical Biology*, *5*, 257–262. <https://doi.org/10.1080/10292389109380405>
- Hülse, D., Lau, K. V., van de Velde, S. J., Arndt, S., Meyer, M. K., & Ridgwell, A. (2021). End-Permian marine extinction due to temperature-driven nutrient recycling and euxinia. *Nature Geoscience*, *14*, 862–867. <https://doi.org/10.1038/s41561-021-00829-7>
- Isozaki, Y. (1997). Permo-Triassic boundary superanoxia and stratified superocean: Records from lost deep sea. *Science*, *276*(5310), 235–238. <https://doi.org/10.1126/science.276.5310.235>
- Kipp, M. A., & Tissot, F. L. H. (2022). Inverse methods for consistent quantification of seafloor anoxia using uranium isotope data from marine sediments. *Earth and Planetary Science Letters*, *577*, 117240. <https://doi.org/10.1016/j.epsl.2021.117240>
- Knoll, A., Bambach, R. K., Payne, J., Pruss, S., & Fischer, W. (2007). Paleophysiology and end-Permian mass extinction. *Earth and Planetary Science Letters*, *256*, 295–313. <https://doi.org/10.1016/j.epsl.2007.02.018>
- Knoll, A. H., Bambach, R. K., Canfield, D. E., & Grotzinger, J. P. (1996). Comparative Earth history and late-Permian mass extinction. *Science*, *273*, 452–457. <https://doi.org/10.1126/science.273.5274.452>
- Lau, K. V., Lyons, T. W., & Maher, K. (2020). Uranium reduction and isotopic fractionation in reducing sediments: Insights from reactive transport modeling. *Geochimica et Cosmochimica Acta*, *287*, 65–92. <https://doi.org/10.1016/j.gca.2020.01.021>
- Lau, K. V., Maher, K., Altiner, D., Kelley, B. M., Kump, L. R., Lehmann, D., et al. (2016). Marine anoxia and delayed Earth system recovery after the end-Permian extinction. *Proceedings of the National Academy of Sciences*, *113*(9), 2360–2365. <https://doi.org/10.1073/PNAS.1515080113>
- Lau, K. V., Romaniello, S. J., & Zhang, F. (2019). *The uranium isotope paleoredox proxy*. Cambridge University Press. <https://doi.org/10.1017/9781108584142>
- Loriga, C., Neri, C., Pasini, M., & Posenato, R. (1986). Marine fossil assemblages from upper Permian to lowermost Triassic in the western Dolomites (Italy). *Memoire Societe Geologique Italy*, *34*, 5–44.

- Maher, K., Steefel, C. I., DePaolo, D. J., & Viani, B. E. (2006). The mineral dissolution rate conundrum: Insights from reactive transport modeling of U isotopes and pore fluid chemistry in marine sediments. *Geochimica et Cosmochimica Acta*, 70, 337–363. <https://doi.org/10.1016/j.gca.2005.09.001>
- Morford, J. L., & Emerson, S. (1999). The geochemistry of redox sensitive trace metals in sediments. *Geochimica et Cosmochimica Acta*, 63(11/12), 1735–1750. [https://doi.org/10.1016/s0016-7037\(99\)00126-x](https://doi.org/10.1016/s0016-7037(99)00126-x)
- Newby, S. M., Owens, J. D., Schoepfer, S. D., & Algeo, T. J. (2021). Transient ocean oxygenation at end-Permian mass extinction onset shown by thallium isotopes. *Nature Geoscience*, 1–6. <https://doi.org/10.1038/s41561-021-00802-4>
- Payne, J. L., & Clapham, M. E. (2012). End-Permian mass extinction in the oceans: An ancient analog for the twenty-first century? *Annual Review of Earth and Planetary Sciences*, 40, 89–111. <https://doi.org/10.1146/annurev-earth-042711-105329>
- Penn, J. L., Deutsch, C., Payne, J. L., & Sperling, E. A. (2018). Temperature-dependent hypoxia explains biogeography and severity of end-Permian marine mass extinction. *Science*, 362, 1327. <https://doi.org/10.1126/science.aat1327>
- R Core Team. (2020). *R: A language and environment for statistical computing*. R Foundation for Statistical Computing. Retrieved from <https://www.R-project.org/>
- Rampino, M. R., Baransky, E., & Rodriguez, S. (2020). Proxy evidence from the Gartnerkofel-1 core (Carnic Alps, Austria) for hypoxic conditions in the western Tethys during the end-Permian mass-extinction event. *Chemical Geology*, 533, 119434. <https://doi.org/10.1016/j.chemgeo.2019.119434>
- Romaniello, S. J., Herrmann, A. D., & Anbar, A. D. (2013). Uranium concentrations and  $^{238}\text{U}/^{235}\text{U}$  isotope ratios in modern carbonates from the Bahamas: Assessing a novel paleoredox proxy. *Chemical Geology*, 362, 305–316. <https://doi.org/10.1016/j.chemgeo.2013.10.002>
- Romano, C., Goudehand, N., Vennemann, T., Ware, D., Schneebeli-Hermann, E., Hochuli, P., et al. (2013). Climatic and biotic upheavals following the end-Permian mass extinction. *Nature Geoscience*, 6, 57–60. <https://doi.org/10.1038/ngeo1667>
- Sahney, S., & Benton, M. J. (2008). Recovery from the most profound mass extinction of all time. *Proceedings. Biological sciences*, 275(1636), 759–765. <https://doi.org/10.1098/rspb.2007.1370>
- Sepkoski, J. (1981). A factor analytic description of the Phanerozoic marine fossil record. *Paleobiology*, 7(1), 36–53. <https://doi.org/10.1017/s0094837300003778>
- Shen, S. Z., Crowley, J. L., Wang, Y., Bowring, S. A., Erwin, D. H., Sadler, P. M., et al. (2011). Calibrating the end-Permian mass extinction. *Science*, 334(6061), 1367–1372. <https://doi.org/10.1126/science.1213454>
- Soetaert, K., Petzoldt, T., & Setzer, R. W. (2010). Solving differential equations in R: Package deSolve. *Journal of Statistical Software*, 33(9), 1–25. <https://doi.org/10.18637/jss.v033.i09>
- Song, H., Wignall, P. B., Tong, J., Bond, D. P. G., Song, H., Lai, X., et al. (2012). Geochemical evidence from bio-apatite for multiple oceanic anoxic events during Permian-Triassic transition and the link with end-Permian extinction and recovery. *Earth and Planetary Science Letters*, 353(354), 12–21. <https://doi.org/10.1016/j.epsl.2012.07.005>
- Song, H., Wignall, P. B., Tong, J., & Yin, H. (2013). Two pulses of extinction during the Permian–Triassic crisis. *Nature Geoscience*, 6(1), 52–56. <https://doi.org/10.1038/ngeo1649>
- Stanley, S., Hardie, L., & Blaustein, M. K. (1999). *Hypercalcification: Paleontology links plate tectonics and geochemistry to sedimentology* (2nd ed., Vol. 9). <https://www.geosociety.org/gsatoday/archive/9/2/pdf/i1052-5173-9-2-1.pdf>
- Stirling, C. H., Andersen, M. B., Potter, E. K., & Halliday, A. N. (2007). Low-temperature isotopic fractionation of uranium. *Earth and Planetary Science Letters*, 264, 208–225. <https://doi.org/10.1016/j.epsl.2007.09.019>
- Stockey, R. G., Cole, D. B., Planavsky, N. J., Loydell, D. K., Frýda, J., & Sperling, E. A. (2020). Persistent global marine euxinia in the early Silurian. *Nature Communications*, 11, 1804. <https://doi.org/10.1038/s41467-020-15400-y>
- Sun, Y., Joachimski, M. M., Wignall, P. B., Yan, C., Chen, Y., Jiang, H., et al. (2012). Lethally hot temperatures during the early Triassic greenhouse. *Science*, 338, 366–370. <https://doi.org/10.1126/science.1224126>
- Sunnåker, M., Busetto, A. G., Numminen, E., Corander, J., & Foll, M. (2013). Approximate Bayesian computation. *PLoS Computational Biology*, 9, 1002803. <https://doi.org/10.1371/journal.pcbi.1002803>
- Tavakoli, V., & Rahimpour-Bonab, H. (2012). Uranium depletion across Permian-Triassic boundary in Persian Gulf and its implications for paleo-oceanic conditions. *Palaeogeography, Palaeoclimatology, Palaeoecology*, 350–352, 101–113. <https://doi.org/10.1016/j.palaeo.2012.06.019>
- Tissot, F. L. H., Chen, C., Go, B. M., Nazimiec, M., Healy, G., Bekker, A., et al. (2018). Controls of eustasy and diagenesis on the  $^{238}\text{U}/^{235}\text{U}$  of carbonates and evolution of the seawater ( $^{234}\text{U}/^{238}\text{U}$ ) during the last 1.4 Myr. *Geochimica et Cosmochimica Acta*, 242, 233–265. <https://doi.org/10.1016/j.gca.2018.08.022>
- Tissot, F. L. H., & Dauphas, N. (2015). Uranium isotopic compositions of the crust and ocean: Age corrections, U budget and global extent of modern anoxia. *Geochimica et Cosmochimica Acta*, 167, 113–143. <https://doi.org/10.1016/j.gca.2015.06.034>
- Weyer, S., Anbar, A. D., Gerdes, A., Gordon, G. W., Algeo, T. J., & Boyle, E. A. (2008). Natural fractionation of  $^{238}\text{U}/^{235}\text{U}$ . *Geochimica et Cosmochimica Acta*, 72(2), 345–359. <https://doi.org/10.1016/j.gca.2007.11.012>
- Wignall, P. B., Bond, D. P. G., Kuwahara, K., Kakuwa, Y., Newton, R. J., & Poulton, S. W. (2010). An 80 million year oceanic redox history from Permian to Jurassic pelagic sediments of the Mino-Tamba terrane, SW Japan, and the origin of four mass extinctions. *Global and Planetary Change*, 71, 109–123. <https://doi.org/10.1016/j.gloplacha.2010.01.022>
- Wignall, P. B., & Hallam, A. (1992). Anoxia as a cause of the Permian/Triassic mass extinction: Facies evidence from northern Italy and the western United States. *Palaeogeography, Palaeoclimatology, Palaeoecology*, 93, 21–46. [https://doi.org/10.1016/0031-0182\(92\)90182-5](https://doi.org/10.1016/0031-0182(92)90182-5)
- Wignall, P. B., & Twitchett, R. J. (1996). Oceanic anoxia and the end-Permian mass extinction. *Science*, 272, 5265. <https://doi.org/10.1126/science.272.5265.1155>
- Zhang, F., Algeo, T. J., Romaniello, S. J., Cui, Y., Zhao, L., Chen, Z. Q., & Anbar, A. D. (2018). Congruent Permian-Triassic  $\delta^{238}\text{U}$  records at Panthalassic and Tethyan sites: Confirmation of global-oceanic anoxia and validation of the U-isotope paleoredox proxy. *Geology*, 46, 327–330. <https://doi.org/10.1130/G39695.1>
- Zhang, F., Shen, S. Z., Cui, Y., Lenton, T. M., Dahl, T. W., Zhang, H., et al. (2020). Two distinct episodes of marine anoxia during the Permian-Triassic crisis evidenced by uranium isotopes in marine dolostones. *Geochimica et Cosmochimica Acta*. <https://doi.org/10.1016/j.gca.2020.01.032>
- Zhang, G., Zhang, X., Hu, D., Li, D., Algeo, T. J., Farquhar, J., et al. (2017). Redox chemistry changes in the Panthalassic Ocean linked to the end-Permian mass extinction and delayed Early Triassic biotic recovery. *Proceedings of the National Academy of Sciences of the United States of America*, 114, 1806–1810. <https://doi.org/10.1073/pnas.1610931114>

## References From the Supporting Information

- Altiner, D., & Özgül, N. (2001). Carboniferous and Permian of the allochthonous terranes of the central Tauride Belt, southern Turkey. In *PaleoForams 2001, International Conference on Paleozoic Benthic Foraminifera Guidebook* (pp. 1–35).
- Andersen, M. B., Vance, D., Morford, J. L., Bura-Nakić, E., Breitenbach, S. F. M., & Och, L. (2016). Closing in on the marine 238U/235U budget. *Chemical Geology*, *420*, 11–22. <https://doi.org/10.1016/j.chemgeo.2015.10.041>
- Elrick, M., Polyak, V., Algeo, T. J., Romaniello, S., Asmerom, Y., Herrmann, A. D., et al. (2017). Global-ocean redox variation during the middle-late Permian through Early Triassic based on uranium isotope and Th/U trends of marine carbonates. *Geology*, *5*, 163–166. <https://doi.org/10.1130/G38585.1>
- Guoqing, W., & Wenchen, X. (2004). Conodont zonation across the Permian-Triassic boundary at the Xiakou section Hubei Province and its correlation with the global Stratotype section and point of the PTB. *Canadian Journal of Earth Sciences*, *41*, 323–330. <https://doi.org/10.1139/e04-008>
- Holser, W. T., Schönlaub, H., Attrep, M., Boeckelmann, K., Klein, P., Magaritz, M., et al. (1989). A unique geochemical record at the Permian/Triassic boundary. *Nature*, *337*, 39–44. <https://doi.org/10.1038/337039a0>
- Holser, W. T., Schönlaub, H., Boeckelmann, K., Magaritz, M., & Orth, C. (1991). The Permian–Triassic of the Gartnerkofel-1 core (carnic Alps, Austria). Synthesis and conclusions. *Abhandlungen der Geologischen Bundesanstalt*, *45*, 213–232.
- Horacek, M., Richoz, S., Brandner, R., Krystyn, L., & Spötl, C. (2007). Evidence for recurrent changes in Lower Triassic oceanic circulation of the Tethys: The  $\delta^{13}C$  record from marine sections in Iran. <https://doi.org/10.1016/j.palaeo.2006.11.052>
- Jinnan, T., Jingxun, Z., & Chen, Z. Q. (2007). Early Triassic carbon isotope excursions from South China: Proxies for devastation and restoration of marine ecosystems following the end-Permian mass extinction. *Geological Journal*, *42*, 371–389. <https://doi.org/10.1002/gj.1084>
- Lehrmann, D. J., Stepchinski, L., Altiner, D., Orchard, M., Montgomery, P., Enos, P., et al. (2015). An integrated biostratigraphy (conodonts and foraminifers) and chronostratigraphy (paleomagnetic reversals, magnetic susceptibility, elemental chemistry, carbon isotopes and geochronology) for the Permian-Upper Triassic strata of Guandao section, Nanpanjiang Basin, south China. *Journal of Asian Earth Sciences*, *108*, 117–135. <https://doi.org/10.1016/j.jseaes.2015.04.030>
- Lehrmann, D. J., Wei, J., & Enos, P. (1998). Controls on facies architecture of a large Triassic carbonate platform: The great bank of Guizhou, Nanpanjiang Basin, South China. *Journal of Sedimentary Research*, *68*, 311–326. <https://doi.org/10.2110/jsr.68.311>
- Noordmann, J., Weyer, S., Sharma, M., Georg, B., Rausch, S., & Bach, W. (2012). Fractionation of  $^{238}U/^{235}U$  during weathering and hydrothermal alteration. *Mineralogical Magazine*, *75*, 1548.
- Richoz, S., Krystyn, L., Baud, A., Brandner, R., Horacek, M., & Mohtat-Aghai, P. (2010). Permian-Triassic boundary interval in the Middle East (Iran and N. Oman): Progressive environmental change from detailed carbonate carbon isotope marine curve and sedimentary evolution. *Journal of Asian Earth Sciences*, *39*, 236–253. <https://doi.org/10.1016/j.jseaes.2009.12.014>
- Sedlacek, A. R. C., Saltzman, M. R., Algeo, T. J., Horacek, M., Brandner, R., Foland, K., & Denniston, R. F. (2014).  $^{87}Sr/^{86}Sr$  stratigraphy from the Early Triassic of Zal, Iran: Linking temperature to weathering rates and the tempo of ecosystem recovery. *Geology*, *42*, 779–782. <https://doi.org/10.1130/G35545.1>
- Shen, J., Algeo, T. J., Hu, Q., Zhang, N., Zhou, L., Xia, W., et al. (2012). Negative C-isotope excursions at the Permian-Triassic boundary linked to volcanism. *Geology*, *40*, 963–966. <https://doi.org/10.1130/G33329.1>
- Zhang, F., Romaniello, S. J., Algeo, T. J., Lau, K. V., Clapham, E. M., Richoz, S., et al. (2018). Multiple episodes of extensive marine anoxia linked to global warming and continental weathering following the latest Permian mass extinction. *Science Advances*, *4*, e1602921. <https://doi.org/10.1126/sciadv.1602921>
- Zhao, L., Chen, Y., Chen, Z. Q., & Cao, L. (2013). Uppermost Permian to lower Triassic conodont zonation from three Gorges area, south China. *PALAIOS*, *28*, 523–540. <https://doi.org/10.2110/palo.2012.p12-107r>
- Zhao, L., Xiong, X., Yang, F., Wang, Z., & He, W. (2005). Conodonts from the lower Triassic in the Nantuowan section of Daxiakou, Xingshan County: Hubei Province. *Albertiana*, *33*, 113–115.